Understanding AlInP(001) Surfaces from Massively Parallel Ab-initio Simulations

I. A. Ruiz Alvarado, L. J. Glahn, M. Krenz, A. Bocchini, K. L. Franzke, U. Gerstmann, and W. G. Schmidt

Abstract Total-energy and electronic structure calculations based on density-functional theory are performed in order to determine the atomic structure and electronic properties of $Al_{0.5}In_{0.5}P(001)$ surfaces. It is found that most of the stable surfaces obey the electron counting rule and are characterized by surface atom dimerization. The dimer related surface states are predicted to occur in the vicinity of the bulk band edges. For a very narrow range of preparation conditions, ab initio thermodynamics predicts metal atomic wires formed by surface cations. In case of typical metalorganic vapor-phase epitaxy growth conditions, a surface covered with a monolayer of buckled phosphorus dimers, where half of the phosphorus atoms are hydrogen-saturated, is found to be stable. This structure also reproduces nicely the reflectance anisotropy measured for epitaxially grown AlInP(001) surfaces.

1 Introduction

III-V compound semiconductors are important for various electronic and optoelectronic applications, e.g., high-electron-mobility transistors, light-emitting diodes, photodetectors, electro-optic modulators, and frequency-mixing components. Solar cells made of III-V semiconductors reach the highest efficiencies of any photovoltaic technology so far [1]. The $Al_xIn_{1-x}P$ (AlInP) material system is frequently used as window layer in solar cells, due to its favorable combination of chemical stability, sufficiently wide bandgap, and high quality heteroepitaxial interfaces with many absorbers [2]. In this context, the Fermi level pinning due to AlInP surface states is highly relevant for the device performance [3]. This holds also for the usage of AlInP as intermediate layer to form low resistance ohmic contacts [4].

However, there is little information available on the atomic structure and electronic properties of AlInP surfaces. It has been noted that different growth conditions lead to different degrees of CuPt ordering in the bulk material [5, 6], i.e., alternating group

I. A. Ruiz Alvarado · L. J. Glahn · M. Krenz · A. Bocchini · K. L. Franzke · U. Gerstmann · W. G. Schmidt (✉)
Lehrstuhl für Theoretische Materialphysik, Universität Paderborn, Paderborn, Germany
e-mail: W.G.Schmidt@upb.de

T. Ludwig et al. (eds.), *High Performance Computing in Science and Engineering '23*,
https://doi.org/10.1007/978-3-031-91312-9_11

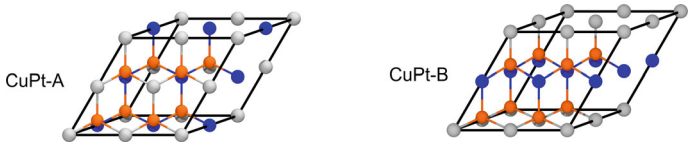

Fig. 1 $Al_{0.5}In_{0.5}P$ bulk material with cations arranged in CuPt-A and CuPt-B symmetry. Gray, blue, orange and white balls represent Al, In, P, and H atoms, respectively

III layers perpendicular to the $[\bar{1}11]$ or $[1\bar{1}1]$ directions, see Fig. 1. This is likely to be related to the formation of surface dimers, which induce strain in the material [7]. Very recently, some models for clean AlInP(001) surfaces were established, which show that structures different from the ones known from binary III-V(001) surfaces may occur [8]. However, this study was restricted to clean surfaces. Often, AlInP is grown by metal organic vapor phase epitaxy (MOVPE) and chemical beam epitaxy (CBE). Since hydrogen is present in MOVPE and CBE, it can be expected to be present at the AlInP surface as well [9, 10].

Therefore, we here extend the previous study [8] to account for the possibility of surface adsorbed hydrogen. A systematic search for stable $Al_{0.5}In_{0.5}P(001)$ surface structures is performed, where the existence of hydrogen is considered as an additional degree of freedom. The initial geometries for structure optimization are generated by systematically varying the surface stoichiometry of both CuPt-A and CuPt-B type ordered $Al_{0.5}In_{0.5}P$ crystals.

Reflectance anisotropy spectroscopy (RAS), also known as reflectance difference spectroscopy [11], is a powerful tool to characterize surfaces at the atomic level: The measurement of the polarization-dependent reflectivity provides insight in the surface structural and electronic properties [12–15]. RAS is non-destructive and can be used in a wide range of environments. It has been used already to monitor the growth of ternary III-V surfaces and heterostructures [16–20]. The understanding and interpretation of the RAS spectra, however, requires numerical simulations. Therefore, RAS spectra are calculated here for the surface structures most relevant in the surface phase diagram.

2 Theory and Implementation

In detail, density-functional theory (DFT) calculations are performed using the Vienna ab initio simulation package (VASP) [21]. The generalized gradient approximation (GGA) with the PBE functional [22] is used to model the electron exchange and correlation interaction. The electron-ion interaction is described by the projector-augmented wave (PAW) scheme [23, 24]. The electronic wave functions are expanded into plane waves up to a kinetic energy cutoff of 400 eV. The Brillouin zone integration is performed using Γ-centered in an equivalent $8 \times 8 \times 1$ mesh in the full (1×1) surface Brillouin zone. The (001) surfaces are modeled by supercells contain-

ing 13 and 14 atomic layers for cation and anion terminated surfaces, respectively, and a vacuum region of ∼13.5 Å. The slab bottom dangling bonds are saturated with fractionally charged H atoms. The electric field resulting from the inequivalence of the two surfaces is taken into account by a dipole correction to the electrostatic potential. The atoms are structurally relaxed until they experience forces smaller than 0.02 eV/Å. The calculations are performed at the equilibrium lattice parameter of $Al_{0.5}In_{0.5}P$ calculated to be 5.751 Å.

In order to compare the various clean and hydrogen covered surfaces energetically, the chemical potentials μ_{A_i} of the respective surface constituents need to be taken into account. The surface ground state is determined by the minimum of the thermodynamic potential

$$\Omega = U - TS - \sum_i \mu_{A_i} n_{A_i}, \tag{1}$$

where U is the total energy of the system. In solids, the entropy term, TS, contributes very little to the difference in Ω under usual experimental conditions [25] and is neglected in the following. The chemical potentials μ_{A_i} for A_i = In, Al, and P are restricted by their bulk values

$$\mu_{A_i} \leq \mu_{A_i,\text{bulk}}. \tag{2}$$

Additionally, the stability of $Al_{0.5}In_{0.5}P$ requires

$$\begin{aligned} \mu_{\text{Al}} + \mu_{\text{In}} + 2\mu_{\text{P}} &= \mu_{\text{AlInP}_2,\text{bulk}} \\ &= \mu_{\text{Al,bulk}} + \mu_{\text{In,bulk}} + 2\mu_{\text{P,bulk}} \\ &\quad -\Delta H_{f,\text{AlInP}_2}. \end{aligned} \tag{3}$$

This allows for formulating the formation energy in dependence on $\Delta\mu_{\text{In}}$ and $\Delta\mu_{\text{Al}}$, i.e., the variations of the In and Al chemical potentials with respect to their bulk values. For the heat of formation $\Delta H_{f,\text{AlInP}_2}$ we calculate a value of −1.49 eV.

The hydrogen chemical potential provides an additional and independent degree of freedom. In the approximation of a two-atomic ideal gas, it is written in dependence on partial pressure p and temperature T as

$$\mu_{\text{H}}(p,T) = \frac{k_B T}{2}\left[\ln\{\frac{p\lambda^3}{k_B T}\} - \ln Z_{\text{rot}} - \ln Z_{\text{vib}}\right] - \frac{1}{2}U_{\text{H}_2}, \tag{4}$$

where k_B is the Boltzmann constant, λ the de Broglie thermal wavelength of the H_2 molecule,

$$\lambda = \sqrt{\frac{2\pi\hbar^2}{mk_B T}}, \tag{5}$$

and Z_{rot} and Z_{vib} are its rotational and vibrational partition functions, respectively. By increasing the temperature, the hydrogen chemical potential is lowered, i.e. less

energy is gained by taking a H atom out of the reservoir and attaching it to the surface. A variation of the hydrogen chemical potential with respect to its molecular value at zero temperature of $\Delta\mu_{\mathrm{H}} \sim -0.6$ eV corresponds, e.g., to the growth conditions in Ref. [26].

DFT calculations typically underestimate the band gap due to the inaccurate treatment of the electronic self-energy. On the DFT level of theory we calculate a band gap of 1.26 eV for CuPt-ordered AlInP bulk, severely underestimating the experimental value of 2.31 eV [27]. Using self-consistent GW calculations [28], we obtain a value much closer to experiment, 2.33 eV. In addition to self-energy effects, optical spectra are affected as well by local-field and electron-hole attraction effects. They are included here by solving the Bethe-Salpeter Equation (BSE) [29–31]. For numerical reasons, we use a model dielectric function in the BSE [32, 33] and approximate the GW quasiparticle shifts by a scissors operator. This methodology leads to an AlInP bulk dielectric function in very good agreement with experiment, as shown in Fig. 2.

Following Refs. [13, 35–37], the reflectance anisotropy is obtained as

$$\frac{\Delta r}{r}(\omega) = \frac{4\omega}{c}\Im\left[\frac{2\pi\Delta\alpha^{hs}(\omega)}{\varepsilon_b(\omega) - 1}\right], \tag{6}$$

where $\varepsilon_b(\omega)$ is the AlInP bulk dielectric function and $\Delta\alpha^{hs}(\omega)$ is the difference of the diagonal tensor elements of the half-slab polarizability corresponding to the respective polarization directions. The calculation of $\Delta\alpha^{hs}$ using a supercell approach contains necessarily not only the surface optical anisotropy, but also contributions from the hydrogen-passivated bottom layer. Fortunately, these contributions are small and occur only for photon energies above 3.5 eV. We get rid of these artifacts by averaging the half-slab polarizabilities for slabs terminated with hydrogen bonds oriented along [110] and [$\bar{1}$10].

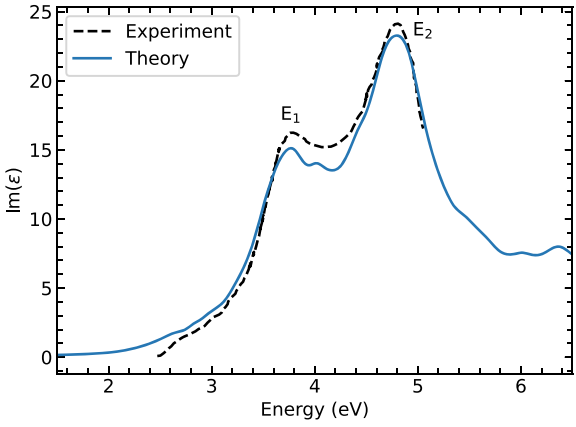

Fig. 2 Imaginary part of the dielectric function of AlInP calculated within the BSE and from experiment [34]

3 Computational Performance

Highly customizable parallelization schemes are implemented in VASP. In particular, parallelization (and data distribution) over bands, parallelization (and data distribution) over plane wave coefficients, as well as parallelization over k-points (no data distribution) can to be used at the same time on massively parallel systems such as the HPE Apollo (Hawk), in order to obtain high computational efficiency.

The performance of Hawk in combination with the available parallelization routines has been tested and optimized with VASP and a test system consisting of 1728 electrons distributed over 1280 orbitals of different symmetry.

The first step of the parallelization procedure is the distribution of the workload related to each orbital on a certain number of cores. It turns out that a number of cores corresponding approximately either to the square root of all available cores or to the total number of cores per node works best for the HRLS Hawk. In addition, this method significantly improves the stability due to reduced memory requirements. Numerical results for the test configuration are shown in Fig. 3 (blue line). This setup results in an improvement up to roughly 2048 cores.

Within the described approach for parallel computing, it is possible to steer the data distribution mode. In particular, the plane wise data distribution in real space can be activated. This allows for a much reduced communication during the Fourier transforms (FFTs). Unfortunately, the resulting load balancing is worsened. Therefore, the suitability of the plane wise data distribution must be tested for the particular computational architecture and in dependence of the number of processors. The results of our tests without plane wise data distribution in real space are shown in Fig. 3 (orange line). As expected, advantages of the plane wise data distribution occur for a relatively small numbers of processors, but are outweighted by load-balancing problems for calculations that employ 4096 cores.

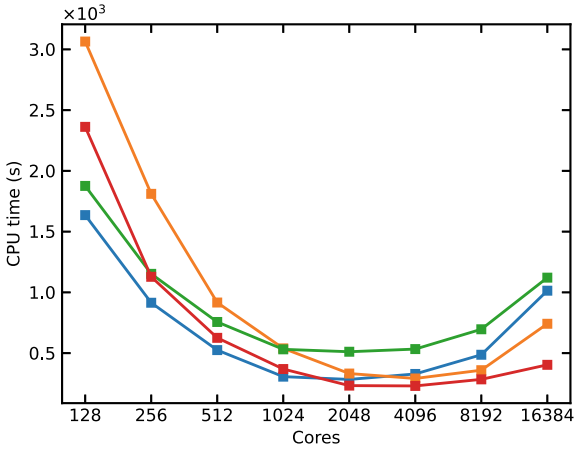

Fig. 3 CPU time on the HRLS Hawk for the self consistent calculation of the electronic structure of a test system consisting of 1728 electrons distributed over 1280 orbitals. See text for details

The computational techniques for the modeling of atomic system discussed here rely on mathematical libraries, in particular the Linear Algebra Package LAPACK or its distributed-memory implementation ScaLAPACK. The calculations discussed above have been performed with ScaLAPACK. This speeds up the calculations by up to a factor of two compared to LAPACK calculations, shown by the green line in Fig. 3. Even if only 128 cores are used, there is a noticeable speed up achieved by using the scalable linear algebra package.

With VASP it is possible to use additionally a parallelization over the k points used to sample the Brillouin zone in the reciprocal space calculations. Thereby it is possible to specify the number of k points that are to be treated in parallel. Within the group of cores that share the work for an individual k point also the electronic states and/or plane wave coefficients are treated in parallel. The results of the corresponding tests are shown in Fig. 3 (red line). It can be seen that the k point parallelization leads to an additional saving of computer time, provided more than 1024 cores are used. The speed up with respect to calculations without k point parallelization amounts up to a factor two. Moreover, this approach allows for the extension of the improved performance up to 4096 cores.

4 Results

4.1 Surface Phase Diagram

Figure 4 contains the calculated phase diagram of the $Al_{0.5}In_{0.5}P(001)$ surfaces structures considered here. Only 10 out of the more than 80 candidate structures considered in our work turn out to be energetically relevant. Schematic top views of these surfaces are compiled in Fig. 5. At hydrogen-deficient conditions ($\Delta\mu_H \sim -1$ eV), P-dimer structures known from clean III-V(001) surfaces [38, 39] dominate the phase diagram. This concerns the c-4×4 structure for anion-rich surfaces, and the β2–2×4 surface for intermediate preparation conditions. The occurrence of [110] oriented P dimers in the P-rich c-4×4 structure and of $[\bar{1}10]$ oriented dimers in 2×4 surface reconstructions is in accord with MOVPE-grown AlInP surfaces in N_2 atmosphere [5]. Hetero-dimer structures featuring either In-P or Al-P dimers in the topmost layer occur for cation-rich preparation conditions. They differ from the mixed-dimer structure known from InP(001) by the staggered arrangement of the second-layer cation dimers, due to the size mismatch between Al and In.

For a broad range of intermediate values of the hydrogen chemical potential, $\Delta\mu_H \sim -0.2 \cdots -0.8$ eV, the 2D-2H surface is found to be stable. It corresponds to a 2×2 reconstructed surface formed by P dimers, see Fig. 5. Hydrogen is adsorbed in an alternating sequence on these buckled P dimers. Similar structures were observed for the (001) surface of InP, GaP, and $In_xGa_{1-x}P$ prepared by gas phase epitaxy [9, 10, 40]. The P dimers of the 2×2-2D-2H surface break up at extremely H-rich conditions, $\Delta\mu_H \sim 0$ eV. In this case, the surface P atoms are alter-

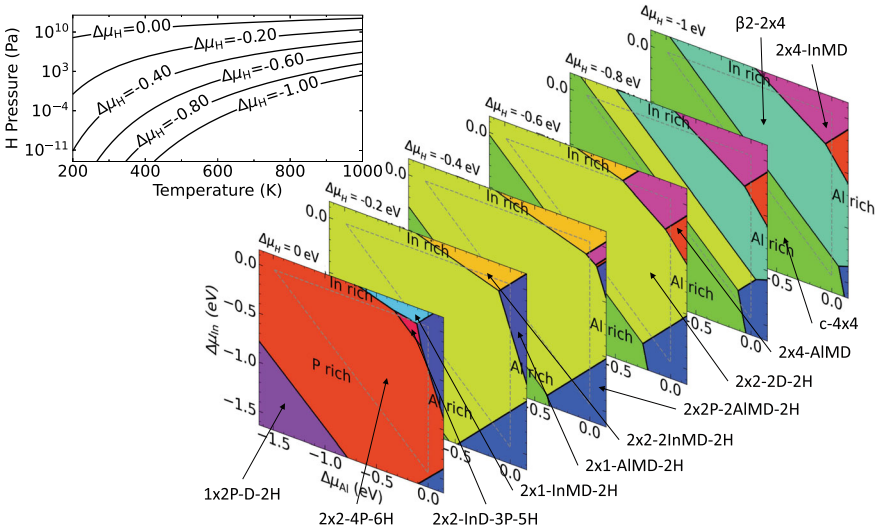

Fig. 4 Energetically favored $Al_{0.5}In_{0.5}P(001)$ surface structures, see Fig. 5, in dependence on the Al, In and H chemical potentials. The thermodynamically allowed range of the chemical potentials according to Eqs. 2 and 3 is indicated by dashed lines. The inset shows the dependence of the hydrogen chemical potential on temperature and partial pressure according to Eq. 4

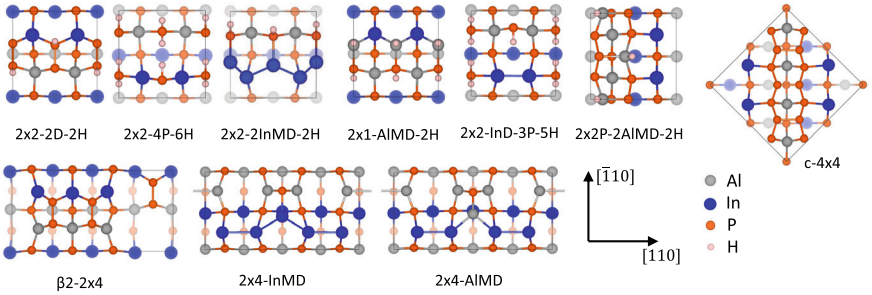

Fig. 5 Top view of stable relaxed clean as well as hydrogenated $Al_{0.5}In_{0.5}P(001)$ surface structures identified in the present work

natingly decorated by one and two hydrogens, forming the 2×2-4P-6H structure. The hydrogen-covered surface P atoms are replaced by H-decorated In-P and Al-P hetero-dimers, if the surface is prepared in hydrogen and cation-rich conditions.

Zunger et al. [41] suggested that the creation of a subsurface selectivity for occupation by a small cation under the strained anion dimer rows, and occupation by a large cation underneath the opening between dimer rows is the main thermodynamic driving force for CuPt ordering in GaInP alloys. The present calculations support this picture for AlInP. All stable P-dimer structures identified here are characterized by P dimers that form above Al, while In occupies the corresponding subsurface

positions between the P-dimer rows, see Fig. 5. No such correlation is found for the hetero-dimer structures. Mixed anion-cation dimers form on top of In, e.g., in the 2×2-2InMD-2H structure, as well as above Al, e.g., in the 2×1-AlMD-2H structure. This agrees with the observation that the degree of atomic ordering of MOVPE-grown AlInP depends sensitively on the preparation conditions [5].

4.2 Surface Electronic Properties

Binary III-V surface reconstructions can be understood in terms of a simple electron counting model (ECM) [42]: A surface structure satisfies this model if all cation dangling bonds are empty and all anion dangling bonds are full, given the number of available electrons. This model may be extended to hydrogen-covered surfaces [43] and is satisfied by the majority of the stable ternary surface structures identified here. In fact, the 2×1-AlMD-2H structure is the only exception to the ECM. It is stable in a very narrow range of preparation conditions that are both cation and hydrogen rich.

Not only is the 2×1-AlMD-2H structure the only stable structure that does not comply with the ECM. It is also the only structure that gives rise to a metallic band structure, see Fig. 6. It features one-dimensional Al-In atomic wires along the [110] direction, which are partially H decorated. The Al-In metal bonds result in a quasi-one-dimensional electron band, which disperses along the atomic wire direction and pins the Fermi energy at mid-gap position. Similar electronic properties are calculated for the 2×2-2InMD-2H structure. Here, an In-In atomic wire extends along the [110] direction and gives rise to two strongly dispersive electron bands. These two bands, one occupied and one empty, are separated by a small band gap of about 0.2 eV and pin the Fermi energy at mid-gap position. However, these two structures are stable

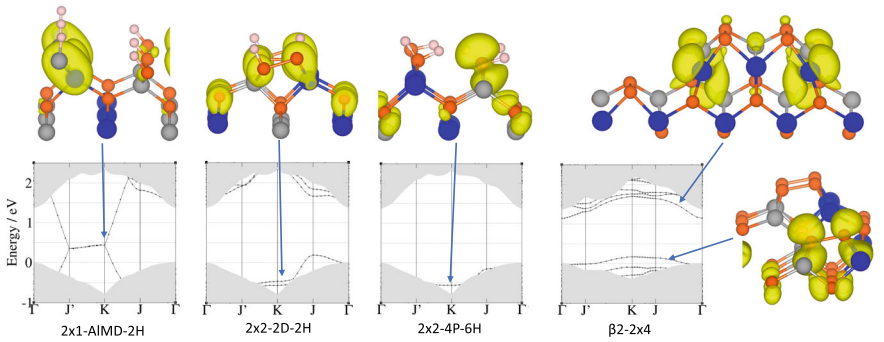

Fig. 6 Band structures of the thermodynamically most relevant surface structures as well as of the 2×1-AlMD-2H surface. Grey regions indicate the projected bulk band structure. ΓJ and ΓJ' are parallel to [$\bar{1}$10] and [110], respectively. The orbital character of state (at the K point) is indicated for prominent surface states. See Fig. 5 for notation of atoms

only in a very small window of preparation conditions, where the cation-rich surface is exposed to hydrogen.

The $\beta 2$–2×4, the 2×2-4P-6H, and, in particular the 2×2-2D-2H structures are far more prominent in the calculated surface phase diagram. They correspond to P-rich surfaces without hydrogen, in extremely hydrogen-rich, and at intermediate conditions, respectively. In case of the 2×2-2D-2H structure, an occupied bound surface state is observed that extends slightly above the bulk valence band maximum (VBM), see Fig. 6. This state is mainly related to the dangling bonds on the up atom of the phosphorus dimer. Exposing the P-rich AlInP(001) surface to very hydrogen-rich conditions leads to the 2×2-4P-6H structure and removes essentially all surface states from the band gap region. In fact, the only remaining surface state occurs at about 0.2 eV below the bulk VBM and corresponds to dangling bonds at under-coordinated surface P atoms. In case of the hydrogen-free $\beta 2$–2×4 surface, an occupied surface state is observed at about 0.2 eV above the bulk VBM. This only weakly dispersive feature corresponds to an anti-bonding π^* combination of p_z orbitals localized at the third-layer P dimer. Additionally, an empty surface state extends slightly into the region of the bulk band gap. It is related to empty dangling bonds located at the three-fold coordinated second-layer cations. It is mainly In localized, but also has some Al contribution.

Generally, with the exception of the 2×1-AlMD-2H and 2×2-2InMD-2H structures discussed above, it is found that all stable surfaces are characterized by occupied surface states close to the bulk VBM that are derived from surface anions or anion-cation-bonds. The unoccupied surface states occur close to the bulk conduction band minimum and are cation related.

4.3 Surface Optical Properties

In Fig. 7 RAS spectra simulated for energetically relevant surface structure models are shown. Obviously, the calculated spectra are highly surface specific. This demonstrates that RAS is suitable to discriminate between the various stable AlInP surface structures and may be used for growth monitoring. Among the structures considered here, best agreement with experiment [44] is found for the 2D-2H surface model. It is the only model that reproduces the pronounced negative feature at 2.5 eV. Given that the 2D-2H surface is also the most dominating structure in the calculated surface phase diagram and that it is consistent with the measured low-energy electron diffraction and X-ray photoelectron spectroscopy data [26], it can be concluded that the AlInP(001) surface produced in the MOVPE environment is composed of a complete layer of phosphorus dimers. Half of the P dangling bonds on the dimers are hydrogen saturated, and the other half are filled with lone pairs of electrons.

While the surface with a 2D-2H reconstruction is stable for a wide range of growth conditions, there occur also other structures in the calculated AlInP(001) surface phase diagram [26]. The 4P-6H surface, see Fig. 5, stable for very H-rich conditions, features six hydrogens bonded to the topmost four P atoms in the surface

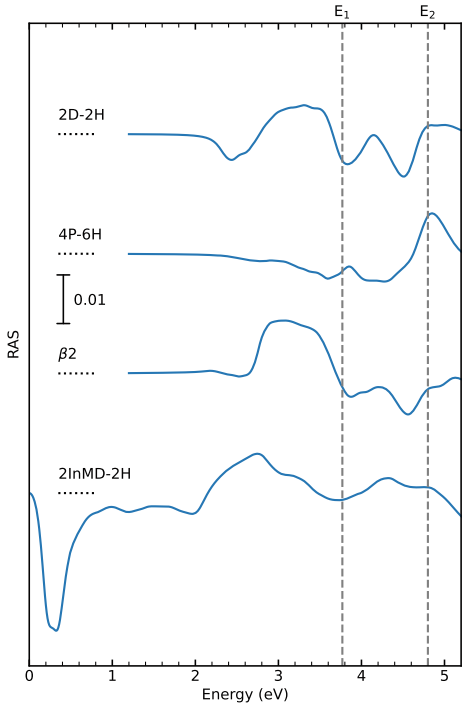

Fig. 7 RAS spectra calculated for energetically relevant surface structure models, see also Fig. 5. The 2InMD-2H spectrum is calculated on the DFT level of theory

unit cell. The hydrogen termination removes essentially all surface states from the AlInP band gap region, see Fig. 6. Accordingly, no significant RAS features appear for low photon energies, see Fig. 7. The optical anisotropies at around 3.8 and 4.8 eV coincide with bulk critical point energies and are likely to be related to surface-modified bulk electronic states [45].

The $\beta 2$ surface, known from various binary III-V compounds, is stable for hydrogen-poor conditions. It is characterized by occupied surface states around the bulk valence band maximum that are due to antibonding π^* combinations of p_z orbitals localized at the P dimer atoms. Electronic transitions from these dimer states into unoccupied surface resonances as well as transition from occupied surface resonances into empty sp^2 orbitals at threefold coordinated surface cations cause a series of positive RAS features between 2.5 and 4.5 eV, see Fig. 7.

Another very interesting structure is formed for a small range of H-rich and In-rich conditions. It consists of In atomic wires that form along the [110] direction. The band structure of this 2InMD-2H surface features two bands, one occupied, one empty, that strongly disperse in wire direction, but have nearly no dispersion perpendicular to the wire direction. These two bands are separated by only about 0.3 eV along the $J' - K$ direction of the surface Brillouin zone and pin the Fermi energy at midgap position. Transitions between these two bands give rise to an extremely strong optical anistropy for low photon energies, see Fig. 7. Similar findings are reported for other surface atomic wire systems [46].

5 Conclusions

In summary, both ab initio thermodynamics as well as the calculated surface optical anisotropy strongly suggest that InAlP(001) surfaces produced in the MOVPE environment are terminated by a complete layer of phosphorus dimers. Half of the P dangling bonds on the dimers are hydrogen saturated, and the other half are filled with lone pairs of electrons. These lone pairs form a bound surface state slightly above the valence band maximum. The calculations suggest the existence of further structures, depending on the surface preparation conditions. P-rich surfaces are characterized by P dimers, while Al-P and In-P hetero-dimers form for more cation-rich surface preparation conditions. Most stable surface structures obey the electron counting rule. Dimer-related surface states are found close to the bulk valence band maximum. Exposure of the surface to extreme hydrogen-rich conditions is predicted to quench the dimerization and to remove all surface states from the region of the bulk band gap. For cation- and hydrogen-rich preparation conditions, metal atomic wires may form on the surface. They give rise to quasi-one-dimensional surface bands that pin the Fermi energy in the mid gap region. These metal atomic wires are predicted to give rise to very strong optical anisotropies.

Acknowledgements The Höchstleistungs-Rechenzentrum Stuttgart (HLRS) is acknowledged for grants of high-performance computer time. Financial support by DFG (PAK981) is gratefully acknowledged.

References

1. Kalogirouo, S.A. (ed.): McEvoy's Handbook of Photovoltaics: Fundamentals and Applications. Academic Press (2017)
2. Kim, C.W., Park, G.Y., Shin, J.C., Kim, H.J.: Appl. Sci. **12**(2) (2022)
3. Lepkowski, D.L., Kasher, T., Boyer, J.T., Chmielewski, D.J., Grassman, T.J., Ringel, S.A.: IEEE J. Photovolt. **10**(3), 758 (2020)
4. Iwata, K., Asahi, H., Ogura, T., Sumino, J., Gonda, S., Ohki, A., Kawaguchi, Y., Matsuoka, T.: In: Seventh International Conference on Indium Phosphide and Related Materials, pp. 183–186 (1995)
5. Jinghua, Z., Xiaohong, T., Jinghua, T.: CrystEngComm **11**(6), 1068 (2009)
6. Yuan, W., Hall, D.C.: J. Appl. Phys. **113**(10), 103515 (2013)
7. Zhang, S.B., Froyen, S., Zunger, A.: Appl. Phys. Lett. **67**(21), 3141 (1995)
8. Ruiz Alvarado, I.A., Karmo, M., Runge, E., Schmidt, W.G.: ACS Omega **6**(9), 6297 (2021)
9. Schmidt, W.G., Hahn, P.H., Bechstedt, F., Esser, N., Vogt, P., Wange, A., Richter, W.: Phys. Rev. Lett. **90**, 126101 (2003)
10. Hahn, P.H., Schmidt, W.G., Bechstedt, F., Pulci, O., Del Sole, R.: Phys. Rev. B **68**, 033311 (2003)
11. Aspnes, D.E., Studna, A.A.: Phys. Rev. Lett. **54**, 1956 (1985)
12. Weightman, P., Martin, D.S., Cole, R.J., Farrel, T.: Rep. Prog. Phys. **68**, 1251 (2005)
13. Schmidt, W.G.: Phys. Status Solidi (b) **242**, 2751 (2005)
14. May, M.M., Lewerenz, H.J., Hannappel, T.: J. Phys. Chem. C **118**(33), 19032 (2014)

15. Lastras-Martínez, A., Ortega-Gallegos, J., Guevara-Macías, L.E., Nuñez-Olvera, O., Balderas-Navarro, R.E., Lastras-Martínez, L.F., Lastras-Montaño, L.A., Lastras-Montaño, M.A.: APL Mater. **2**(3), 032107 (2014)
16. Zorn, M., Jönsson, J., Krost, A., Richter, W., Zettler, J.T., Ploska, K., Reinhardt, F.: J. Cryst. Growth **145**(1–4), 53 (1994)
17. Haberland, K., Bhattacharya, A., Zorn, M., Weyers, M., Zettler, J.T., Richter, W.: J. Electron. Mater. **29**(4), 468 (2000)
18. Krahmer, C., Philippens, M., Schubert, M., Streubel, K.: Phys. Status Solidi c **3**(3), 655 (2006)
19. Krahmer, C., Philippens, M., Schubert, M., Streubel, K.: J. Cryst. Growth **298**, 18 (2007)
20. Supplie, O., Heinisch, A., Sugiyama, M., Hannappel, T.: In: 2018 IEEE 7th World Conference on Photovoltaic Energy Conversion (WCPEC) (A Joint Conference of 45th IEEE PVSC, 28th PVSEC & 34th EU PVSEC), pp. 3923–3926. IEEE, Waikoloa Village, HI (2018)
21. Kresse, G., Furthmüller, J.: Comp. Mat. Sci. **6**, 15 (1996)
22. Perdew, J.P., Burke, K., Ernzerhof, M.: Phys. Rev. Lett. **77**, 3865 (1996)
23. Blöchl, P.E.: Phys. Rev. B **50**, 17953 (1994)
24. Kresse, G., Joubert, D.: Phys. Rev. B **59**, 1758 (1999)
25. Wippermann, S., Schmidt, W.G.: Phys. Rev. Lett. **105**, 126102 (2010)
26. Glahn, L.J., Ruiz Alvarado, I.A., Neufeld, S., Zare Pour, M.A., Paszuk, A., Ostheimer, D., Shekarabi, S., Romanyuk, O., Moritz, D.C., Hofmann, J.P., Jaegermann, W., Hannappel, T., Schmidt, W.G.: Phys. Status Solidi (b) **259**(11), 2200308 (2022)
27. Cheong, J.S., Ng, J.S., Krysa, A.B., Ong, J.S.L., David, J.P.R.: J. Phys. D Appl. Phys. **48**(40), 405101 (2015)
28. Shishkin, M., Marsman, M., Kresse, G.: Phys. Rev. Lett. **99**(24), 246403 (2007)
29. Albrecht, S., Reining, L., Del Sole, R., Onida, G.: Phys. Rev. Lett. **80**(20), 4510 (1998)
30. Rohlfing, M., Louie, S.G.: Phys. Rev. Lett. **81**(11), 2312 (1998)
31. Schmidt, W.G., Glutsch, S., Hahn, P.H., Bechstedt, F.: Phys. Rev. B **67**, 085307 (2003)
32. Bechstedt, F., Del Sole, R., Cappellini, G., Reining, L.: Solid State Commun. **84**(7), 765 (1992)
33. Liu, P., Kim, B., Chen, X.Q., Sarma, D.D., Kresse, G., Franchini, C.: Phys. Rev. Mater. **2**(7), 075003 (2018)
34. Ochoa-Martínez, E., Barrutia, L., Ochoa, M., Barrigón, E., García, I., Rey-Stolle, I., Algora, C., Basa, P., Kronome, G., Gabás, M.: Sol. Energy Mater. Sol. Cells **174**, 388 (2018)
35. del Sole, R.: Solid State Commun. **37**(7), 537 (1981)
36. Del Sole, R., Fiorino, E.: Phys. Rev. B **29**(8), 4631 (1984)
37. Manghi, F., Del Sole, R., Selloni, A., Molinari, E.: Phys. Rev. B **41**(14), 9935 (1990)
38. Schmidt, W.G.: Appl. Phys. A **65**, 581 (1997)
39. Schmidt, W.G.: Appl. Phys. A **75**, 89 (2002)
40. Cheng, S.F., Sun, Y., Law, D.C., Visbeck, S.B., Hicks, R.F.: Surf. Sci. **600**(14), 2924 (2006)
41. Bernard, J.E., Froyen, S., Zunger, A.: Phys. Rev. B **44**, 11178 (1991)
42. Pashley, M.D.: Phys. Rev. B **40**, 10481 (1989)
43. Karmo, M., Ruiz Alvarado, I.A., Schmidt, W.G., Runge, E.: ACS Omega **7**(6), 5064 (2022)
44. Ruiz Alvarado, I.A., Zare Pour, M.A., Hannappel, T., Schmidt, W.G.: Phys. Rev. B (submitted)
45. Schmidt, W.G., Bernholc, J.: Phys. Rev. B **61**, 7604 (2000)
46. Chandola, S., Hinrichs, K., Gensch, M., Esser, N., Wippermann, S., Schmidt, W.G., Bechstedt, F., Fleischer, K., McGilp, J.F.: Phys. Rev. Lett. **102**(22), 226805 (2009)